Journal of Materials Research and Technology 36 (2025) 9262–9273

Contents lists available at ScienceDirect

Journal of Materials Research and Technology

journal homepage: www.elsevier.com/locate/jmrt

Suppression of Cr nanoclusters and enrichments in Fe–Cr based alloys with cryogenic processing for future energy sector

Matic Jovičević-Klug [a,1], Carlo Alberto Brondin [b,1], Antonio Caretta [c], Carsten Bonnekoh [d], Florian Gossing [e], Alexandra Vogel [a], Michael Rieth [d], Jeffrey McCord [e], Michael Rohwerder [a], Patricia Jovičević-Klug [a,f,*,1]

[a] Max Planck Institute for Sustainable Materials GmbH, Max-Planck-Straße 1, 40237, Düsseldorf, Germany
[b] Istituto di Struttura della Materia (ISM), ISM), Consiglio Nazionale delle Ricerche (CNR), 34149, Trieste, Italy
[c] Elettra- Sincrotrone Trieste S.C.p.A, Strada Statale 14 - km 163,5 in AREA Science Park, 34149, Basovizza, Italy
[d] Institute for Applied Materials, Karlsruhe Institute of Technology, Hermann-von-Helmholtz-Platz 1, 76344, Eggenstein-Leopoldshafen, Germany
[e] Nanoscale Magnetic Materials, Institute of Materials Science, Kiel University Kaiserstraße 2, 24143, Kiel, Germany
[f] Alexander von Humboldt PostDoc Research Fellow, Alexander von Humboldt Foundation, Jean-Paul-Straße 12, 53173, Bonn, Germany

ARTICLE INFO

Keywords:
Fe–Cr alloy
Cryogenic processing
Cr clusters
Micro-residual stress
Magnetism
Mechanical behaviour

ABSTRACT

This study investigates the effect of cryogenic processing (CP) on the microstructure and properties of a steel, Eurofer97, being considered for application in the energy sector - fusion. Relatively simple microstructural tailoring with CP provides a novel route to advanced steels for the energy sector, utilizing existing alloys and chemistry. The resulting microstructural changes provide improved microhardness of the material and altered micro-residual stresses to a more compressive nature. The study shows that CP modifies the microstructural evolution immediately after application and during tempering. Magnetic characterisation was carried out using magneto-optical Kerr effect (MOKE) microscopy, a versatile technique for imaging magnetic domains and evaluating the behaviour of magnetic materials. Temperature-dependent magneto-optical characterizations were carried out in ultra-high vacuum MOKE, ranging from cryogenic to elevated temperatures, to avoid thermal-induced reactions in ambient pressure. The combined investigation of magnetic properties and microstructural features elucidates the clear formation of carbides over intermetallic enrichment zones that stabilizes the microstructure. This pioneering work carried out provides important research for the application of CP for the development of next generation metallic materials for current and future energy sectors.

1. Introduction

Eurofer97 belongs to the group of reduced activation ferritic-martensitic (RAFM) steels, which are of great interest for being the main material for the construction of the first wall of future fusion reactors [1,2]. The correlation between microstructure and final properties such as magnetic properties, mechanical properties, corrosion properties, etc. is critical to the application and longevity of Eurofer97. Previous studies have shown that Eurofer97 presents a strong correlation between microstructure parameters (grain/particle size, dislocation density, particle spacing, influence on residual stress development, plastic deformation and dislocation distribution) [2,3]), magnetic behaviour (saturation, magnetization, exchange energy and intrinsic magnetic anisotropy [2,4,5]), and mechanical behaviour ((micro)hardness, toughness and strength [3,5–8]). The interrelations between microstructure and material properties are critical aspects when the material is exposed to neutrons, as the microstructure can be altered during exposure in a fusion reactor. These radiation-induced microstructural changes directly influence the final properties that in specific cases can be critical to the material stability, leading to embrittlement and failure of reactor components [2,9]. Studies showed that irradiation of Eurofer97 causes that alloying elements (C, Cr, Mn, N etc.) at

* Corresponding author. Max Planck Institute for Sustainable Materials GmbH, Max-Planck-Straße 1, 40237, Düsseldorf, Germany.
E-mail addresses: m.jovicevic-klug@mpie.de (M. Jovičević-Klug), carloalberto.brondin@trieste.ism.cnr.it (C.A. Brondin), antonio.caretta@elettra.eu (A. Caretta), carsten.bonnekoh@kit.edu (C. Bonnekoh), flgo@tf.uni-kiel.de (F. Gossing), a.vogel@mpie.de (A. Vogel), michael.rieth@kit.edu (M. Rieth), jmc@tf.uni-kiel.de (J. McCord), rohwerder@mpie.de (M. Rohwerder), p.jovicevic-klug@mpie.de (P. Jovičević-Klug).
[1] These authors contributed equally to the manuscript.

https://doi.org/10.1016/j.jmrt.2025.05.176
Received 4 February 2025; Received in revised form 9 April 2025; Accepted 19 May 2025
Available online 20 May 2025

dislocations are driven by strain energy relief, which can also cause the segregation of alloying elements at these dislocations, leading to local dealloying and formation of embrittled regions [10–12].

In order to stabilise the Eurofer97 microstructure for withstanding the exposure to high energy particles during its usage, various heat treatment/processing techniques and different chemical compositions are applied to maximise the performance and durability of Eurofer97 [13–15]. One of the options is Cryogenic Processing (CP), where the material is exposed to cryogenic temperatures as part of CP, usually below 77 K, for a period of time to modify the material's microstructure and nanoscopic features and thus its final properties [16–26]. Many studies have demonstrated a positive influence of CP on alloys and improvement of various properties. However, despite the positive promises of the new processing method, there is a perceived lack of research in this area, particularly in regards to the mechanisms that drive the individual changes in these specific steels. Previous studies by Jovičević-Klug et al., 2024a [17], 2024b [16] and 2024c [27] have demonstrated that CP alters the microstructure and oxidation dynamics of alloying elements, which has been shown to increase the corrosion and surface resistance of Eurofer97. To our best knowledge, there are no other studies on the testing of Eurofer97 and CP. There are some studies that perform and test mechanical behaviour, magnetic behaviour and observe microstructural changes of stainless and RAFM steels in cryogenic temperatures [28–30], which is not the same as processing them in these extreme temperatures. But there are studies on other steels, which were cryogenically processed and tested in regards to their magnetic behaviour and properties [28,31–33].

Furthermore, advanced magnetic studies of CP on materials used in the energy sector have never been carried out to observe the in-situ and in-operando behaviour of the material. Therefore, it is necessary to make an in-depth study of the effect of CP on Eurofer97 in terms of induced changes in microstructure and final properties. This is particularly of interest in relating the underlying sub-micrometre microstructural features and defects to the magnetic domain structures and overall magnetic properties that can serve as indicators and tracing figure of merits for selected properties.

This study focuses on the effect of heat treatments with varying tempering temperature and exposure to cryogenic processing on the microstructure (including macro-residual stresses), magnetic and mechanical behaviour of Eurofer97. Furthermore, in this study one of the first observations with advanced synchrotron measurements of the magnetic behaviour of Eurofer97 in relation to CP is tested, presented and interpreted.

2. Methods

2.1. Material, processing, microstructure and phase analysis

Eurofer97/2 is a Cr-rich Fe alloy (chemical composition in wt.%: 0.11C, 0.4 Mn, 9 Cr, 0.12 Ta, 1.1 W, 0.03 N, 0.15 V, base Fe, other alloying elements <0.012). A plate (heat 993394) with 9.2 mm (nominal 8 mm) thickness was supplied by the Karlsruhe Institute of Technology (KIT), Germany [13]. The plate was provided in the as manufactured condition, i.e., after rolling, a heat treated was conducted at Böhler Bleche GmbH: 980 °C for 14 min, air quenched, 760 °C for 90 min and finally air cooled. Eurofer97 samples were firstly divided into six sub-groups, control (C1, C2, C3) and test groups (T1, T2, T3). The test groups were exposed to cryogenic processing, where three different heat treatments were applied on the selected subgroups as presented in Table 1. The temperature of austenitisation was fixed at T_a = 1000 °C/0.5 h and a quenching rate (800-500 °C) of ~10 °C/s was achieved. Afterwards the control subgroups were subjected to 1 cycle of tempering, whereas the test subgroups were subjected to CP followed by 1 cycle of tempering.

All samples were heat treated at the Max Planck Institute for Sustainable Materials (MPI SusMat), Germany. All specimens were heat treated in an Ar atmosphere under high vacuum. This was done to eliminate the influence of N_2 gas on the microstructure during hardening and tempering. Samples were metallographically prepared for further analysis according to Jovičević-Klug et al., 2021 [34] for the preparation of cryogenically processed ferrous alloys. The microstructural analysis of the Eurofer97 alloy was performed using a Zeiss Crossbeam Merlin I scanning electron microscope (SEM) at MPI SusMat.

Table 1
Heat treatment parameters of all subgroups, where CX are control groups with no CP application, and TX are test groups with CP.

Sample Group	Austenitisation temperature (T_a in °C)	Cryogenic processing (CP=24 h at -196 °C)	Tempering temperature (T_t in °C)
C1	1000/0.5 h	No	350/2 h
T1	1000/0.5 h	Yes	350/2 h
C2	1000/0.5 h	No	450/2 h
T2	1000/0.5 h	Yes	450/2 h
C3	1000/0.5 h	No	550/2 h
T3	1000/0.5 h	Yes	550/2 h
TaQ	1000/0.5 h	No	No
TaQCP	1000/0.5 h	Yes	No

For quantitative phase analysis, XRD scans were performed using a Rigaku SmartLab diffractometer with a Cu K_α X-ray source. The diffractometer is equipped with a micro area beam optic (500 μm by 500 μm beam size), a 5-circle goniometer and a HyPix3000 area detector. The measurements were performed as a continuous symmetrical overview scan with a step size of $\Delta 2\Theta = 0.01°$, a scan rate of 4°/min and a power setup of 45 kV/200 mA. The measured data were used to quantify the individual phases using Rietveld simulation.

2.2. Micro-residual stress measurements

The micro-residual stress measurements were carried out using a Rigaku SmartLab with a Cu Kα rotating anode X-ray source. The diffractometer is equipped with a micro area beam optic (beam size 500 μm by 500 μm), a 5-circle goniometer, and a HyPix3000 area detector. For each sample a residual stress measurement was done for the major phases (weight fraction >10 %). The 2Θ position of a reflex selected for the respective phase was measured for 13 different sample tilts ($-63.5° \geq \chi \geq +63.5°$), for three different stress directions ($\Theta = 0°$, $\Theta = 45°$ and $\Theta = 90°$) each. The 2Θ position there used to calculate the residual stress according the $\sin^2\psi$-method [35].

2.3. Thermodynamic modelling

Thermodynamic modelling was conducted in order to understand ratio and formation of phases during exposure to cryogenic temperatures followed by the tempering. It was performed with Thermo-Calc Software using TCFE11 database and MOBFE6 database.

2.4. Mechanical behaviour testing

2.4.1. Microhardness

Microhardness of samples obtained after different heat treatment procedures was measured using Vickers HV30 method at room temperature (21 °C and 50 % humidity). For each subgroup multiple measurements were performed on several specimens (at least 6) and the average value was calculated.

2.4.2. Impact toughness

The evolution of Charpy energy was measured utilizing a pendulum machine (ZwickRoell) with a capacity of 25 J and an instrumented fin with a tip radius of 1 mm. The testing machine was equipped with a specimen magazine and a conditioning box for heating/cooling the specimens to the aimed test temperature. Heating/cooling and

subsequent testing was conducted in air. Miniaturized V-notch Charpy specimens (KLST) 27 × 4x3 mm in size were used, which are described in DIN EN ISO 14556:2017–05 Figure D1. The orientation of the crack system for all specimens was L-T; cf. ASTM E399-19 Fig. 1 for the definition of directions in plate samples. Outer specimen geometry as well as the V-notch were machined by electrical discharge machining. Testing the KLST specimens was conducted as follows: (1) The specimens were loaded into the magazine; (2) In the control software, a test temperature was assigned to each specimen in the magazine. (3) At the start of the test program, the first KLST specimen was automatically transferred to the conditioning box for heating/cooling. (4) After a dwell time of 2 min the specimen was transferred from the conditioning box to the test position and the pendulum was released. The temperature change that took place during the transfer from the conditioning box to the test position was compensated in advance by heating/cooling the specimen in the conditioning box slightly above/below the aimed test temperature. Following the test of the first specimen the second KLST specimen was fed to the conditioning box, the pendulum returned to the release position. After completion of the test campaign, the lateral extension of the fractured and unfractured specimens was determined; cf. DIN EN ISO 148–1:2017-05 Figure B1. The inspection of the samples was conducted with an optical microscope Keyence VHX7000.

2.5. Magnetic behaviour testing

2.5.1. Atom force microscopy – mode magnetic force microscopy

Atomic force microscopy (AFM) with a measurement mode magnetic force microscopy (MFM) was used to measure the static magnetic domain structure of the investigated samples. This non-contact scanning force method directly measures the presence and distribution of inherent magnetic fields emitted by the remanent magnetic domain states. Magnetic domains are imaged by measuring magneto-static interactions between the tip (30 % Ni and 70 % Fe) and the sample during slow scanning of the cantilever over the sample surface [36]. The AFM-MFM measurements were carried out in the Cypher Environmental System from Oxford Instruments in a dry N_2-gas environment.

2.5.2. Magneto-optical Kerr effect microscopy

For microscale resolved imaging of present magnetic structures magneto-optical Kerr effect (MOKE) microscopy is carried out. Here a modified high-resolution bright-field microscope setup with polarization optics is used. This setup includes a high-power LED as the light source and an electromagnet to apply homogeneous magnetic fields to the sample. By eccentrically positioning the light source in the back focal plane, longitudinal MOKE sensitivity is achieved [37]. Differential imaging is used to extract the weak MOKE contrast [38]. Furthermore, to reduce the effect of sample displacement due to the applied external magnetic field, images are acquired by switching from positive to negative fields as described by Jovičević-Klug et al., 2021 [31] and 2022 [39]. Additional image postprocessing is carried out in order to remove the topographical and illumination artefacts as described in Ref. [31].

2.5.3. UHV MOKE

Temperature-dependent (from −248 °C to 77 °C) MOKE experiments were carried out at the MAGNEDYN beamline at the FERMI free electron laser [40]. The setup utilized the off-line end station sector dedicated to magnetic experiments. The experimental setup consisted of a stabilized HeNe laser, a mechanical chopper operating at 700 Hz, a high-quality polarizer, the sample, a half-wave plate, a Wollaston polarizer, and a balanced photodetector. The signal from the photodetector was analysed using a lock-in amplifier. The sample was mounted on a closed-loop cryostat and placed between the poles of an external electromagnet. Measurements were performed in longitudinal MOKE geometry, with an angle of incidence of 15° that also has a polar component present in the measurements. Kerr rotation data as a function of the magnetic field were acquired from −248 °C up to 77 °C, with temperature stability maintained at ±1 °C during acquisition. Due to the contraction of the sample holder caused by temperature variations, the vertical position of the sample had to be adjusted during the measurement procedure. An imaging camera was used to minimize the displacement of the laser spot on the sample, with an accuracy of ±200 μm. Temperature-dependent (from RT to 477 °C) MOKE characterization was carried out in another ultra-high vacuum experimental chamber, specifically designed to be coupled with the optical setup for magnetic measurements. A continuous-wave HeNe laser at 633 nm was used as the light source, as the one employed in the MAGNEDYN station. Changes in polarization were determined using a polarization modulation technique involving a photoelastic modulator [41]. Details of the optical layout and the entire system can be found in Ref. [42]. The electromagnet available in the MOKE chamber is capable of generating magnetic fields up to 140 mT. The sample was positioned using a manipulator, allowing measurements in either longitudinal or polar geometry; the measurements presented here were acquired in longitudinal geometry with an angle of incidence of 45°. The temperature of the sample was increased by radiative heating and monitored using a K-type thermocouple attached directly to the sample, and measurements were taken in 50 °C increments. For the analysis of the acquired hysteresis data, data postprocessing was performed in terms of correction of

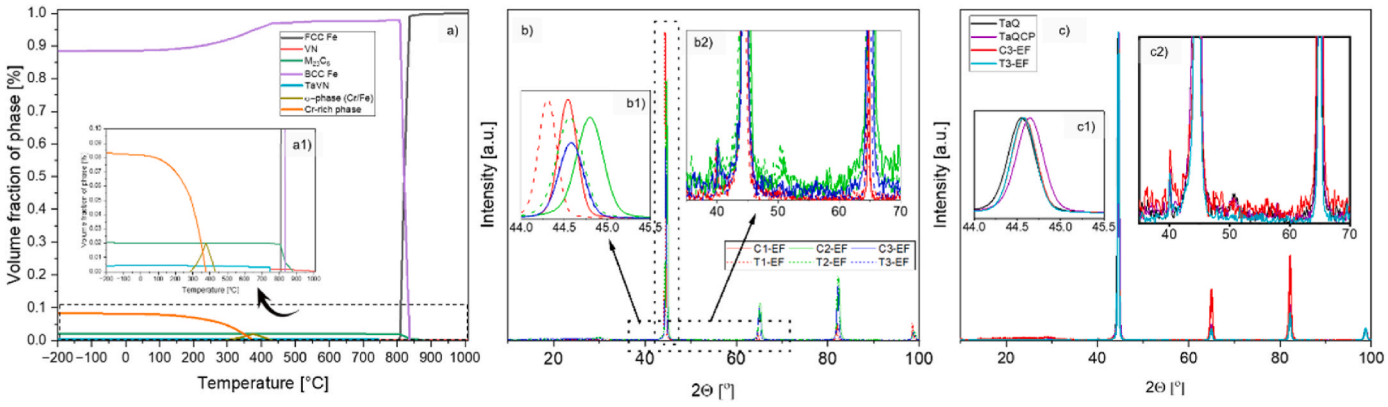

Fig. 1. Parts a & a1 show modelling results of precipitation and formation of phase through changes in temperature from −200 to 1100 °C, insert a1) shows a magnification of the highlighted region. Parts b-b2 show the XRD results of all 6 groups (Cx & Tx), where different tempering temperature and cryogenic processing (CP) was applied. The selected tempering temperatures were 350 °C (C1 & T1 sample groups), 450 °C (C2 & T2 sample groups) and 550 °C (C3 & T3 sample groups). c-c2 parts represent XRD results of the observed microstructural evolution for the last heat treatment with elevated tempering temperature, where after hardening (TaQ sample) and directly after CP (TaQCP) sample were tested in order to observe CP effectiveness on the selected Eurofer97 alloy. For comparison purposes, the intensities of diffractograms in inserts b-b1 and c-c1 were normalized to present the relative displacement of the main peak of the BCC phase along the 2Θ axis.

Faraday rotation and thermal drift [31,43].

3. Results and discussion

3.1. Material description Eurofer97: thermodynamics modelling, microstructure and micro-residual stresses

Thermodynamic modelling (Fig. 1a and a1) predicts precipitation of vanadium nitrides (red curve - VN) after 750 °C and precipitation of tantalum-vanadium nitrides (light blue curve - TaVN) from −200 °C to 750 °C. Formation of the BCC Fe phase (purple curve - ferrite or martensite) occurs up to about 840 °C. From 800 °C onwards the transformation to the FCC Fe phase (black curve - austenite) is present. Precipitation of $M_{23}C_6$ carbides (green curve) is modelled to occur from −200 °C to 850 °C. This type of carbides is not present at selected austenitisation temperature as they dissolve during the transformation from the BCC phase to the FCC phase. Based on the thermodynamic modelling also formation of σ-phase (olive green curve - Cr/Fe phase) is exacted in the range from 285 °C to 430 °C. Under lower temperature conditions, in the range of −200 °C–375 °C, the σ-phase and BCC Fe phase are reformed to a Cr-rich phase (orange curve). Thus, the model indicates the potential of the additional nucleation sites for CP that are related to the prior high-temperature $M_{23}C_6$ carbide phase as well as the potential of retransformation to Cr-rich BCC phase. XRD results (Fig. 1b and c and Fig. 2, Table 2) of the samples showed the presence of BCC phase, FCC phase and Cr-rich BCC phase and precipitation of the following carbides M_3C_2, $M_{23}C_6$, M_6C, M_7C_3 and (V, Ta) nitrides.

Fig. 1b and Table 2 indicate the trend of higher presence of BCC phase in the matrix with higher tempering temperatures in CP samples compared to the control groups (C2 & C3). Then, for all test groups (T1, T2 & T3) the effective transformation of FCC (nonmagnetic phase) into BCC (magnetic phase) has been observed (50–100 % effectiveness of CP according to XRD data). Furthermore, the presence of σ-phase (nonmagnetic phase) is higher in the control groups (C1 & C2) with lower tempering temperature compared to CP groups (T1 & T2). In regards to different types of precipitated carbides (nonmagnetic phase), the XRD and modelling provide and confirm the remarkable observation that after application of CP an increase of $M_{23}C_6$ carbides occurs (300 % C1→T1, 270 % C2→T2 & 260 % C3→T3). This observation is partly confirmed by the mechanism observed by Jovičević-Klug et al., 2020 [44], in which in CP the maternal phase is M_7C_3. However, in this observed case it is proposed that the source of their formation are also

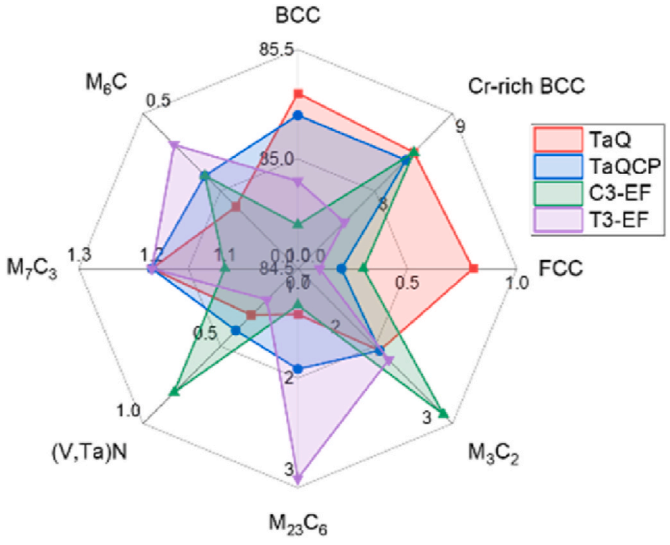

Fig. 2. Spider diagram of groups, which show evolution of microstructure in vol%.

Table 2
XRD results of control (no CP, C1, C2, C3 & TaQ) and test samples (with CP, T1, T2, T3 & TaQCP) in vol%.

Sample	BCC	Cr-rich BCC	FCC	M_3C_2	$M_{23}C_6$	(V, Ta)N	M_7C_3	M_6C
C1	86.5	8.6	0.1	2.2	1.1	0.1	1.1	0.3
T1	86.1	7.3	0	1.6	3.3	0.2	1.2	0.3
C2	84.7	8.7	0.6	2.2	1.3	0.8	1.3	0.4
T2	84.9	7.5	0.2	2.1	3.5	0.3	1	0.5
C3	84.7	8.5	0.3	3.1	1.2	0.8	1.1	0.3
T3	84.9	7.6	0.1	2.5	3.1	0.2	1.2	0.4
Evolution of microstructure								
	BCC	Cr-rch BCC	FCC	M_3C_2	$M_{23}C_6$	(V, Ta)N	M_7C_3	M_6C
TaQ	85.3	8.5	0.8	2.4	1.3	0.3	1.2	0.2
TaQCP	85.2	8.4	0.2	2.4	1.9	0.4	1.2	0.3
C3	84.7	8.5	0.3	3.1	1.2	0.8	1.1	0.3
T3	84.9	7.6	0.1	2.5	3.1	0.2	1.2	0.4

the intermediate M_3C_2 carbides and partially also the σ-phase. In this particular case, the intermediate carbides (M_7C_3 and M_3C_2) are not shown by the thermodynamic equilibrium due to their metastability, but are known as the prior base carbides for the formation of $M_{23}C_6$ and M_6C carbides [44,45]. The subsequent alloying of the carbides and enrichment with metal content is thus insinuated by the interfacial exchange of alloying elements, particularly Cr, between the carbides and the Cr-rich BCC phase. The formation of the Cr-rich BCC phase is associated with the occurrence of a miscibility gap between the Cr-rich BCC phase and the conventional Fe BCC phase, which is associated with spinodal decomposition, as described by Jacob et al., 2018 [46]. In essence, the miscibility gap can be compensated for by a heterogeneous nucleation and growth event of the BCC phase. This forces the desegregated formation of the Cr-rich BCC phase and the Fe BCC phase. This is particularly visible for the C3/T3 case, where the tempering temperature is highly above the transition temperature of the σ-phase, which enables sufficiently enhanced mobility of the Cr as well as other alloying elements from the matrix phase and σ-phase towards the carbides. The proposed role of intermetallic σ-phase for carbide precipitation was suggested by Diegele et al., 2017 [47], but not in correlation to CP. However, the observation of high Cr and Fe intermetallic σ-phase at cryogenic temperature has been observed by Jo et al., 2018 [48] for FCC high entropy alloys (commonly known as HEA) with higher ratio of Cr, Fe, Ni, Co and V, which can be correlated to the observation of Eurofer97, due to the high Cr and Fe content with lower amount of Ni, V and Co. The results corroborate this observation by the lower presence of σ-phase derived Cr-rich BCC in CP samples, further confirming the proposed mechanism and source of Cr and Fe for newly precipitated carbides.

To confirm the mechanism of the CP-enhanced $M_{23}C_6$ carbides formation, the evolution path of the effect of CP on microstructure for the third group (C3/T3) was also monitored to understand the effect of CP on microstructure and consequently on final properties, which is shown on Fig. 1c–c2 and 2 and Table 2. The results of the phases showed that immediately after CP (TaQ is for the sample directly after hardening and TaQCP is sample after hardening and CP before tempering) a slightly lower presence of Cr-rich BCC and significantly lower presence of FCC (by 75 %). Furthermore, the data confirm the mechanism of $M_{23}C_6$ precipitation involved by CP, which showed 38 % increase in their precipitation immediately after CP. After an additional tempering step after CP was carried out to observe the role of CP placement in the heating route. This showed an increase in the BCC phase, a further decrease in the Cr-rich BCC and FCC phases and slight changes in the volume ratio of the precipitates due to segregation of alloying elements and their mobilisation during the high temperature treatment.

Further investigation of microstructure with SEM was done to support the XRD results and, in addition, to observe any morphological changes of the phases (size, refinement, shape etc.) induced by CP in

different groups. The microstructural analysis of samples undergone six different heat treatments is presented in Fig. 3a–f. For all samples, the major phase is confirmed to be in the form of martensitic laths that become coarser with increasing tempering temperature. A more prominent recrystallization occurs for the groups C3/T3, which is associated with the relaxation of the martensitic matrix with tempering temperature exceeding the transformation temperature of σ-phase as determined from thermodynamic calculations (see Fig. 1). Such microstructural changes of Eurofer97 is also supported by previous literature [2,49]. The matrix showed smaller martensitic laths with CP, which was also observed and consistent with our previous studies of Eurofer97 [16,17]. Martensitic laths are smaller in first group C1/T1 by roughly 30 %, in second group C2/T2 by 50 % and in third group C3/T3 by roughly 30 %, corroborating with the results from previous study [17]. The precipitates are mainly present for all samples at the grain boundaries, which is suggested to be correlated to the prior σ-phase that tends to precipitate with austenite destabilisation at prior austenitic grains [50]. The Cr-rich BCC phase is consistently found as smaller grains that accompany the non-enriched martensitic laths. The carbides are majorly found at the grain boundaries, associated to the heterogenous nucleation of the matrix with respect to the prior present carbides. However, as also confirmed in a previous study by Jovičević-Klug et al., 2024 [17] smaller, nanoscopic carbides can precipitate also within martensitic laths as best seen from group C3/T3.

The XRD data clearly show the influence of the CP on the evolution of the lattice misfit/strain, as can be seen from the comparison of the (211) peak of the BCC phase in Fig. 1b–b1. Particularly, it shows how the lower temperature tempering in the case of C1/T1 and C2/T2 has a clear relation to a more compressive-like (reduced tensile) stress state with CP compared to the conventional group. These effects corroborate with the CP inherently allowing the generation of higher compressive stresses associated with to the migration of alloying elements and relaxation of the phase transformation before and after tempering [20,39,51]. Interestingly with the intermediate tempering the compressive character is enhanced with C2, while the stresses are practically compensated in the case of C3 with respect to their conventionally treated group. The higher tempering temperature groups C3/T3 show values of the lattice parameters close to zero-stress nominal values for BCC Fe/ferrite (a =

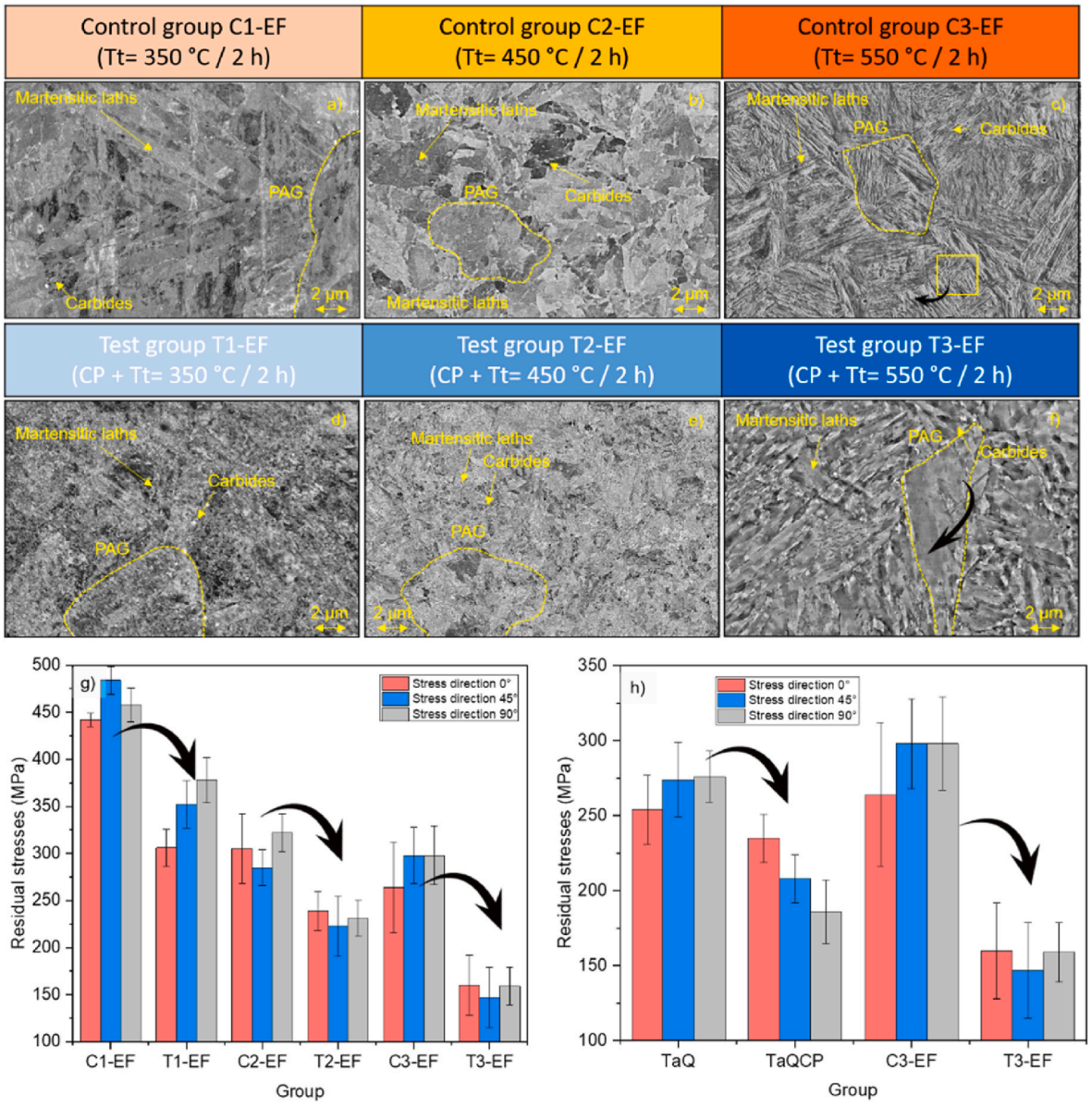

Fig. 3. Micrographs obtained with secondary electrons by scanning electron microscopy (SEM) for control groups a), b) and c), and cryogenically processed groups d), e) and f) of Eurofer97 steel samples. Measured residual stresses of samples (in direction 0°, 45° and 90°) are presented in g) and h) parts.

2.8656 Å) [52]. These results clearly show the active effect of the tempering temperature on the capabilities of CP to compensate the tensile stresses, when it is of sufficient level. This is corroborated by the evolution pathway presented in Fig. 1c–c1, where after quenching we have slight tensile character of the lattice, while after CP without tempering a lower tensile character is developed, but then with tempering the strain characteristics are modified, with C3 being more tensile and T3 more less tensile. It should be noted that these estimates present a general view of the orthogonal lattice strains related to the (211) planes that can effectively be related also to alloying and not to the microscopic overall inherent stress states in the different directions. For the accurate estimation of the stress states, further analysis of the samples is performed via micro-residual stress measurements.

The micro-residual stress measurements (see Supplementary Material 1a & b) helped to provide deeper analysis of reduced tensile stresses with CP, originating from the modified microstructure, as shown in Fig. 3g and h. In all heat treatment groups, the test groups, displayed always lower tensile stresses than their control counterpart. The lowering of the tensile stresses was on average 25 %, 24 % and 45 % for the C1/T1, C2/T2 and C3/T3, respectively. The results also show that with higher tempering temperature the residual stresses are reduced (regardless of presence of CP), which are proportionally further reduced with the intermediate CP (see arrows in Fig. 3g). Generally, no direct relations were identified between the different orientations and the corresponding residual stresses. This suggests that the heat treatments do not develop any clear texture-governed stress evolution. However, a larger disparity between the 0° and 45° against 90° directions was visible for the lower tempering temperature groups (C1/T1 and C2/T2), which could indicate that a weak stress texture could be present for these groups, which goes in hand with the strongly modified ferrite matrix in the case of C3/T3. The most significant change in micro-residual stresses is observed in the third group (C3/T3), this can be correlated, as mentioned above, to the higher number of defects in the crystal lattice with greater change of increased precipitation of precipitates, which was also confirmed by our XRD and SEM analysis. A particularly interesting fact is the subtle change of the residual stress state between C2/C3, while the T2/T3 is considerably stronger, which strongly corroborates with the high effect of CP with higher tempering temperature as observed also for other martensitic stainless steels [19].

In addition to final states and their results of residual stresses also evolution of micro-residual stresses was analysed for the third group (Fig. 3h), where TaQ is for sample directly after hardening and TaQCP is sample after hardening and CP before tempering. The results show as expected that there are high values of tensile residual stresses in the sample directly after hardening, where the values were 254 ± 23 MPa, 274 ± 25 MPa and 276 ± 17 MPa, accordingly. The same sample also exhibits the highest value of FCC phase and Cr-rich BCC compared to other samples in evolution monitoring (Table 2), which explains the highest values of micro-residual stresses. Directly after exposure to CP (sample TaQCP) the stresses are partly transformed into more compressive residual stresses by 7–32 %, respectively. This confirms our previous observation [16,19] that direction of 90° promotes the build-up of more compressive residual stresses and releases of tensile residual stresses. This suggested that 90° direction is the direction with the most potential for occurrence of defects and nucleation site during tempering, which also can correspond to the weak site in regards to chemo-physical-mechanical properties. As observed T3 exhibits more compressive stresses compared to C3, but the most interesting aspect is that C3 and correspondingly then also C2 and C1/T1 develop higher tensile stresses compared to the stress state of the quenched material. This clearly indicates the strong impact of the CP on the evolution and thus also the relation to the development of the residual stress state that cumulatively affects the dimensional stability and resistance to cracking of Eurofer97.

3.2. Mechanical behaviour

3.2.1. Microhardness

From Fig. 4a and b the trend of minor increase of microhardness after application of CP is observed for all heat treatments groups (C1–C3, T1-T3).

The increase of microhardness (Fig. 4a) in the first two groups with the lowest selected tempering temperature (350 °C) (C1/T1) is very minor (~2 %) (from 225 ± 1 HV to 230 ± 2 HV). In the second two groups (C2/T2) with medium selected tempering temperature (450 °C) the highest change of microhardness is observed after application of CP, reaching 5 % from 363 ± 6 HV to 386 ± 11 HV. In the third treatment, the highest selected tempering temperature (550 °C) groups (C3/T3) also experienced a minor increase (~3 %) after application of CP from 353 ± 5 HV to 366 ± 9 HV. Monitoring the evolution of the microstructure (Fig. 4b) after CP showed a very small increase immediately after exposure to CP (TaQCP sample, by ~1 %) from 380 ± 4 HV (TaQ before CP) to 384 ± 6 HV (TaQCP after CP), which is also within the standard deviation of the samples. The samples after tempering had in average lower microhardness value, alto the effect of CP was stronger on the final samples (Fig. 4b). Overall, the trend of increased microhardness seems to follow well the trend of reduced tensile residual stresses, indicating that the general stress state can be related to the strength of the material that is governed by the microstructural changes.

The explanation for the increased microhardness after CP in Eurofer97 is suggested to be correlated to the efficient retained austenite (FCC phase) transformation into BCC phase (especially seen in C2/T2 groups), as seen in the microstructure part and by our previous studies [16,17] in correlation to the Eurofer97. Furthermore, the increase in the microhardness can be also related to the increased nucleation of carbides and transformation of the σ-phase to carbides that inherently also reduces the tensile residual stresses. The explanation of the phenomenon, where the microhardness is lower after tempering, could be attributed to the changes in the matrix, however as seen in the microstructure part, the CP is effective already directly after application, so no major changes are present [16,17,44]. However, the decrease in hardness can in C3 be well correlated to the higher presence of RA and lower presence of $M_{23}C_6$ carbides. In T3 the increase in the hardness can be nicely correlated not only to the matrix, but also to the evolution of $M_{23}C_6$ [44] and at the same time, this can explain the lower microhardness after tempering ($M_{23}C_6$ have on average 900–1400 HV microhardness) [53].

Due to the prominent effect of the CP effect on Eurofer97 in the case of the C3 and T3 group and the general trend between the different tempering groups, further detailed investigation was performed only on groups C3, T3, TaQ and TaQCP. This is also particularly sensible based on prior literature that stipulates that no significant softening and massive carbide precipitation is expected to occur up to tempering temperatures of 550 °C [2,49,54,55].

3.2.2. Impact toughness

Fig. 4c–d shows the results of the impact toughness tests using the Charpy method, where Fig. 4c shows the fractographic analysis and Fig. 4d the impact toughness results in J for evolution racking samples (TaQ, TaQCP, C3 and T3). Fractographic analysis (Fig. 4c) of Eurofer97 showed a generally flatter cleavage surface for CP samples (TaQCP and T3) compared to TaQ and C3 samples (no CP), which is suggested to correspond to a more refined BCC phase. Additional observations (Fig. 4 c-1 and c-2) also showed that carbides exhibit cracking, which is more common in CP samples. This is correlated with the higher degree of cohesion for CP samples of the matrix and carbides, which corresponds to the higher resistance to stress cracking of the matrix by dislocation pinning on precipitates. A similar observation for CP effect on impact toughness and cracking was observed for high Cr high speed steels [56]. Based on the residual stress results, the slight preferential pinning of dislocations will be in the 90° direction.

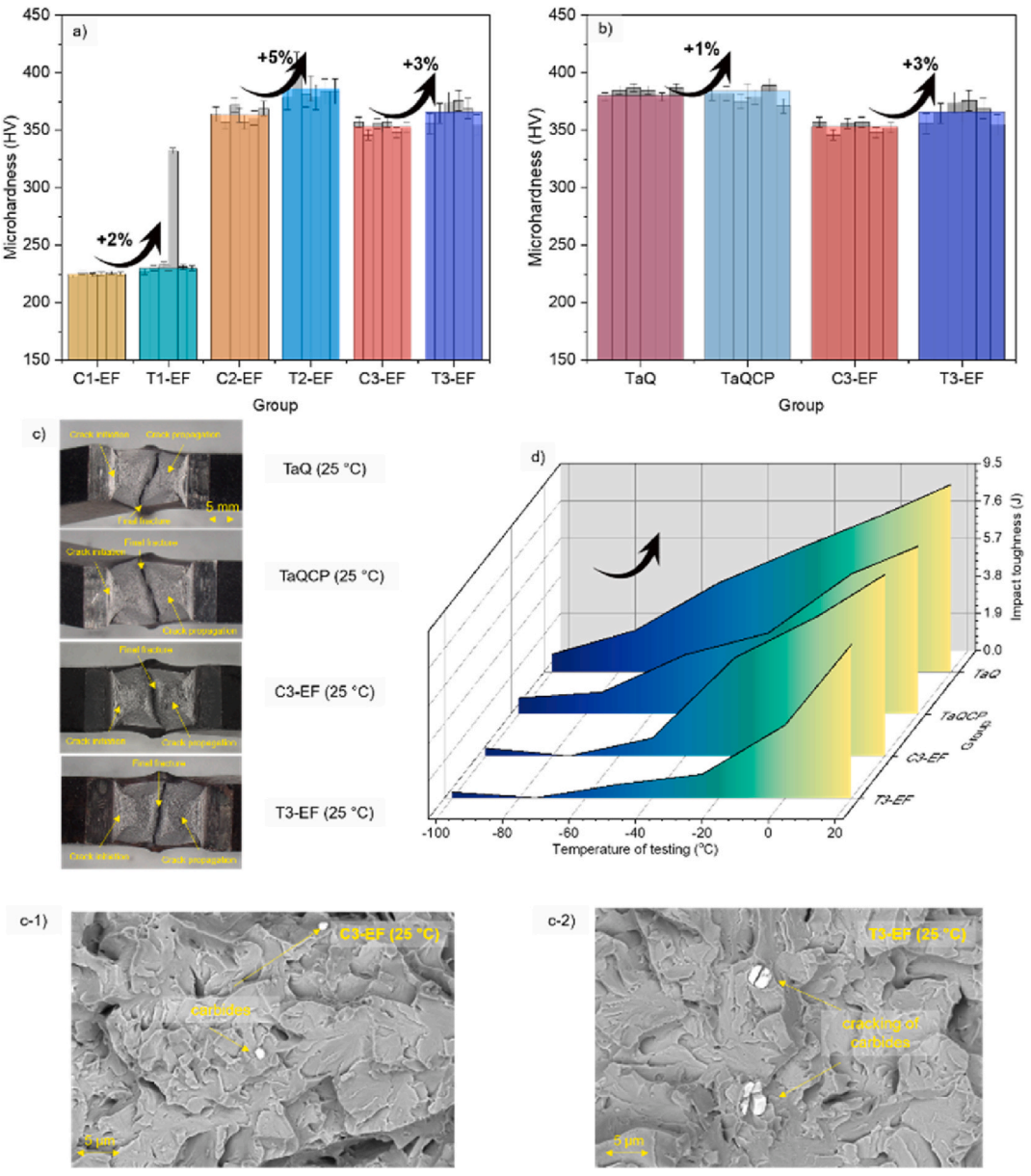

Fig. 4. The results of the microhardness test for all groups a) with noted changes. For each group, six measurements were made to ensure the reproducibility of the results with the standard deviation included. In b) the microhardness of selected samples during heat treatment evolution for the highest tempering temperature, where also six measurements were made with included standard deviation. Part c) represents the selected examples of fractographic analysis of the impact toughness test for four specimens to monitor the effect of CP on the microstructure evolution. Parts c-1 and c-2) represent the SEM images of carbides with lower or no cracking and carbides exhibiting the cracking. Part d) shows the results of the Charpy impact toughness test for the same groups as seen in the c) part. All conditions show a similar upper shelf energy at about 9–10 J.

The testing results of impact toughness (Fig. 4d) showed on average lower impact toughness values (↓~15–100 %) for CP treated selected samples (TaQCP and T3) in different temperature testing environments (−100 °C, −75 °C, −50 °C, −25 °C, 0 °C and 25 °C). At −100 °C testing environment the values of CP were 0.3 ± 0.05 J (T3) and 0.8 ± 0.04 J (TaQCP), accordingly, whereas values for samples without CP were 0.4 ± 0.05 J and 0.9 ± 0.05 J, respectively. The most notable difference in CP samples and without CP samples were at −75 °C (1.1 ± 0.06 J for CP samples and 2.1 ± 0.12 J for samples without CP) and −25 °C (1.2 ± 0.06 J and 4.1 ± 0.21 J for CP samples and 5 ± 0.25 J and 6.3 ± 0.28 J for samples without CP, accordingly), where values were 80–100 % lower in CP samples compared to samples with CP. The lowest difference in the samples were at 25 °C environmental temperature of testing, where values for CP samples were 7.8 ± 0.39 J (T3) and 8.5 ± 0.43 J (TaQCP), respectively. For control samples were 8.4 ± 0.42 J (C3) and 9.5 ± 0.48 J (TaQ), accordingly. Impact toughness is related strongly to the cohesion and composition of the matrix, which is also strongly correlated to the (micro)hardness of the material. The decrease of the toughness can be explained by a slight increase in the microhardness for all CP samples and increase in BCC phase [19,57] that is overall related to the higher amount of carbides and thus higher density of stress concentration points.

3.3. Magnetic characterisation and nanoclustering

The changes in the microstructure, local alloying and stress state can be related to and monitored through the changes in magnetic properties as the local spin-orbital coupling and exchange between the highly magnetic matrix phase and less magnetic carbide and intermetallic phases are directly related to these changes. The overall magnetic

response of the material can be assessed by the magnetic hysteresis measured with magneto optical Kerr microscopy (MOKE), as presented in Fig. 5a. The hysteresis displays an opening from −0.2 to 0.2 T externally applied field (H_{ext}) that indicates spontaneous changes in magnetization related to domain wall motion, whereas at higher fields most magnetization changes occur due to coherent magnetization rotation coupled with local demagnetization effects. For establishing a spatial correlation of the magnetization/magnetic domains to the microstructural features, local magnetic hysteresis (Fig. 5b) and domain imaging (Fig. 5c, c1, c2, c3) was performed on the C3 and T3 samples. To establish a proper relation of the magnetization with the saturation magnetization (M_s), the hysteresis of the MOKE microscopy was normalized based on the hysteresis obtained with a laser setup that enables application of higher magnetic fields to confirm the maximum MOKE contrast related to the M_s of the material (see Fig. 5a). It should be noted that due to the optical geometry of the MOKE setup a polar component is inherently measured, which is slightly visible by the signal change in a form of a peak near $\mu_0 H_{ext} = 0$ T, which is accounted for in the interpretation of the hysteresis.

The magnetic hysteresis of the T3 displays a larger opening compared to C3, as seen from Fig. 5b. The opening effectively reaches coercive fields of 135 mT and 83 mT, for T3 and C3 respectively, while the remanent magnetization is 40 % larger for T3 compared to C3. The overall characteristics of the opening indicate that the grain-to-grain coupling needs to be stronger, which can be attributed to a more Cr-rich boundaries and the simultaneous refinement of the ferrite grains as already determined from the SEM results. Additionally, the coercivity can be enhanced by pinning of the magnetic domain walls by the carbides, especially since the $M_{23}C_6$ carbides, whose numbers increase with CP, display low M_s compared to other Fe-rich carbides found in Eurofer97 [58].The refinement of ferrite grains and the higher coercivity is visible from the MOKE micrographs in Fig. 5c, c1, c2 and c3, which present clearly the finer domain structure of the T3 and the slightly lower change of magnetization with application of H_{ext}. To further present the strong change in remanence and grain-to-grain magnetic coupling with higher spatial resolution, atomic force microscopy with magnetic mode was performed on remnant states of both C3 and T3. The resulting domain structures, presented in Fig. 5, confirm the refined magnetic domain structure even on μm-scale as well as the reduced grain coupling with T3. With the accompanying topographic maps, the domain patterns are shown to clearly extend through several grains, confirming the coupling of the different grains in both samples, but less extensive in T3. The higher-resolution images in d3 and e3, present also clearly that the segmentations of the domains are finer for T3, indicating an inherently higher M_s. The higher field response from the hysteresis corroborates with this, since the hysteresis present a weaker increase in magnetization of T3 compared to C3, indicating a lower susceptibility and thus harder magnetic character of T3. This in turn correlates well with the less tensile residual stresses [59] for T3 compared to C3. This effectively also indicates a slight increase of the M_s with CP. Additionally, the potentially lower alloying of the matrix with Cr with CP due to the formation of a larger amount of carbides can also contribute to increase of the M_s [60]. The different magnetization development with H_{ext} is also presented through MOKE images in Supplementary material 2-5.

Further elucidation of the differences in the magnetic characteristics of the Eurofer97 with CP (sample T3) and with no CP (sample C3) is provided by in-situ hysteresis measurements of the samples during

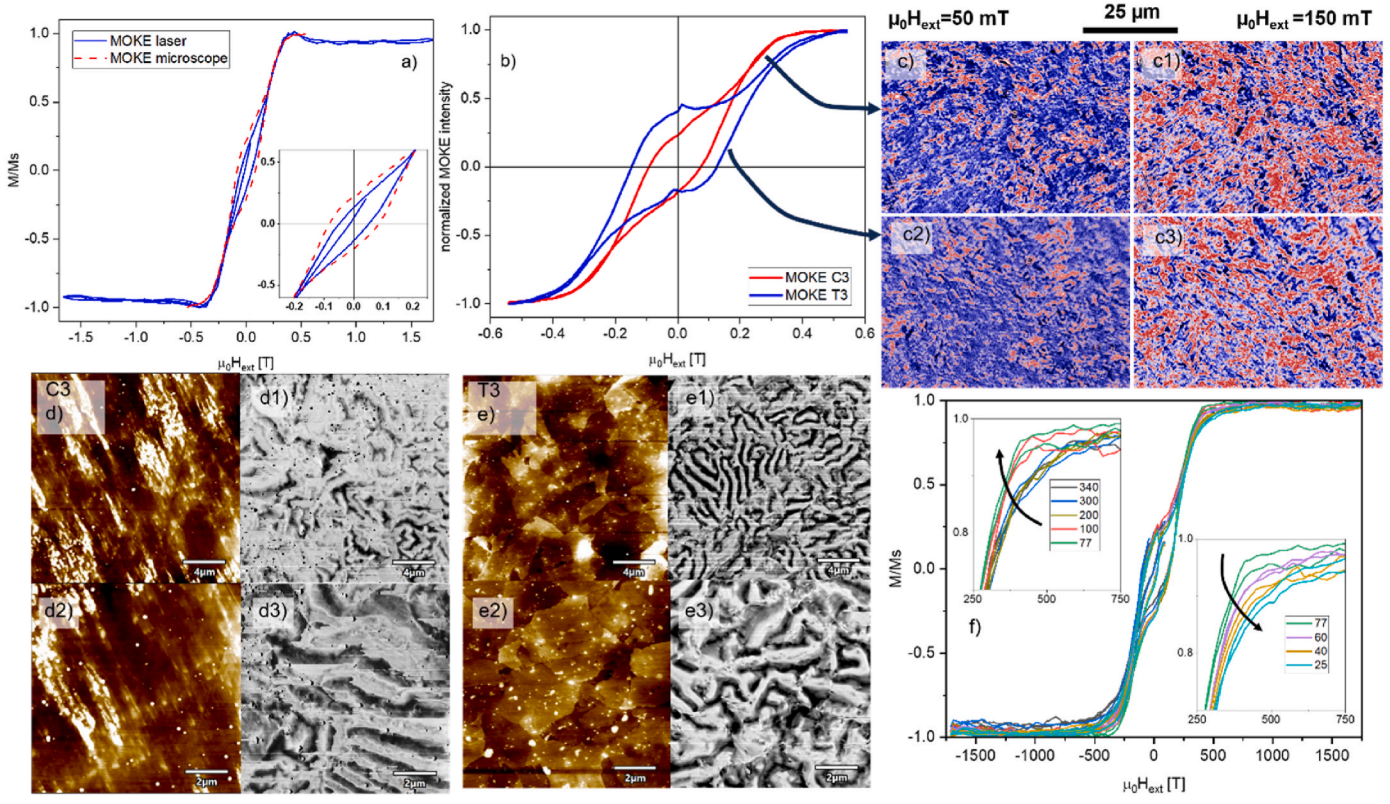

Fig. 5. a) Magnetic hysteresis loop of C3 sample obtained from a MOKE laser-based setup with applied fields (H_{ext}) up to 1.75 T (blue curve) overlapped with hysteresis obtained with MOKE microscope setup with H_{ext} up to 0.6 T (red curve). The insert a1), shows the enlargement of the opening part of the hysteresis. b) Magnetic hysteresis of C3 and T3 obtained with MOKE microscope setup. Overall magnetic domain structure at 2 points in the hysteresis for both C3 (c and c1) and T3 (c2 and c3) color-coded with blue-white-red look-up table. AFM-MFM micrographs of C3 (d1 and d3) and T3 (e1 and e3) with corresponding topographical scans (d and d2) and (e and e2), respectively. The contrast range of the topographical scans is 2 nm between dark and bright contrast. f) Series of magnetic hysteresis obtained during in-situ CP treatment of C3 sample with inserts presenting the individual trends of hysteresis change with temperature (values in K) indicated by arrows in the inserts.

exposure to cryogenic temperatures (down to −248 °C (25 K)). The in-situ results confirm the differences in the hysteresis opening between C3 and T3. However, compared to previous MOKE microscopy extracted hysteresis the opening is larger for C3 than for T3 (see Fig. 5b and compare with Supplementary Material 6) indicating a local dependency of the hysteresis opening that corroborates with the visibility of domain patches seen from MOKE micrographs (Fig. 5c–c3). Additionally, to the hysteresis form, the evolution of the hysteresis of the C3 and T3 with temperature show also clear differences between the samples. In the case of C3, the hysteresis shows a clear modification of the curvature of the hysteresis close to saturation with temperature as presented in Fig. 5f. The modification of the hysteresis follows an initial magnetic softening with decreasing temperature down to −196 °C (77 K), while with even lower temperatures, the trend is reversed, indicating a stepwise hardening of the hysteresis in this field regime (see inserts in Fig. 5). On the other hand, the T3 sample displays no strong changes in this field regime. Furthermore, the T3 hysteresis presents overall significantly lower changes with temperature compared to the C3 hysteresis.

To provide more quantitative relations, the individual parameters of relative M_s, coercive field (H_c) and maximum slope of the hysteresis for both samples was extracted for both C3 and T3 samples as presented in Fig. 6. The M_s (see Fig. 6a) indicates that the relative change of M_s with temperature is lower for T3 than for C3. The diagram also indicates an abrupt change in M_s for C3 at a temperature of about −33 °C (240 K), indicating a discontinuity that could be related to a secondary phase that exhibits a magnetic transition at this temperature. The potential origin of such discontinuity could be the presence of Cr-rich segments that exhibit a Néel transition temperature connected with Cr, as explained in Refs. [61,62]. In turn this could be either explained from the M_s drop originating from the antiferromagnetic coupling of the Cr-rich segments with the Fe-rich matrix (i.e Cr-rich grain boundaries and ferrite grains) or from Cr-nanoclustering in the Fe matrix. This can be theoretically explained by the dominant antiferromagnetic coupling of the Fe–Cr neighbours, which effectively reduce the M_s once the Fe–Cr coupling dominates over the Cr–Cr coupling. In turn this leads to a preferred parallel coupling of the Cr–Cr neighbours that effectively induce a ferromagnetic ordering of the Cr-rich clusters. A theoretical calculation by Fu et al. [63] indicates that under the nanoclustering of Cr in octahedral form, such antiferromagnetic coupling of the cluster to the Fe matrix is a possibility at the temperatures observed in this study. This is also supported by the fact that the relative M_s change after this anomaly follows a similar trend of decreasing M_s with increasing temperature as for T3, which follows Bloch's law and primarily originates from the M_s change of the Fe matrix. Overall, this suggests that the Cr clustering is suppressed in the case of T3 sample due to the CP-induced preferential formation of $M_{23}C_6$ carbides over intermetallic clusters. This proposed theory is also supported by the observed changes in Cr binding with CP measured by scanning photoelectron microscopy and the formation of Cr-rich interfaces and zones by atom probe tomography (APT) from previous studies [16,17,27]. Additional data analysis of the APT data also clearly shows that the carbides in the C3 sample develop a clear Cr-rich layer around pre-existing M_3C_2 and M_7C_3 carbides (see Fig. 6b) that has no correlation with carbon or nitrogen. In contrast the T3 sample clearly exhibits only the formation of carbides with no distinct Cr-rich zones, consistent with the proposed mechanism of suppression of Cr clustering with CP through the formation of fine $M_{23}C_6$ carbides. The study of Cr-enrichment and clustering in Fe–Cr alloy systems by Fedorov et al. [64] corroborates to the formation of Cr clusters in the surrounding of carbides and nitrides. In addition, the same study through Monte Carlo modelling stipulates that the Cr-rich clustering is only possible

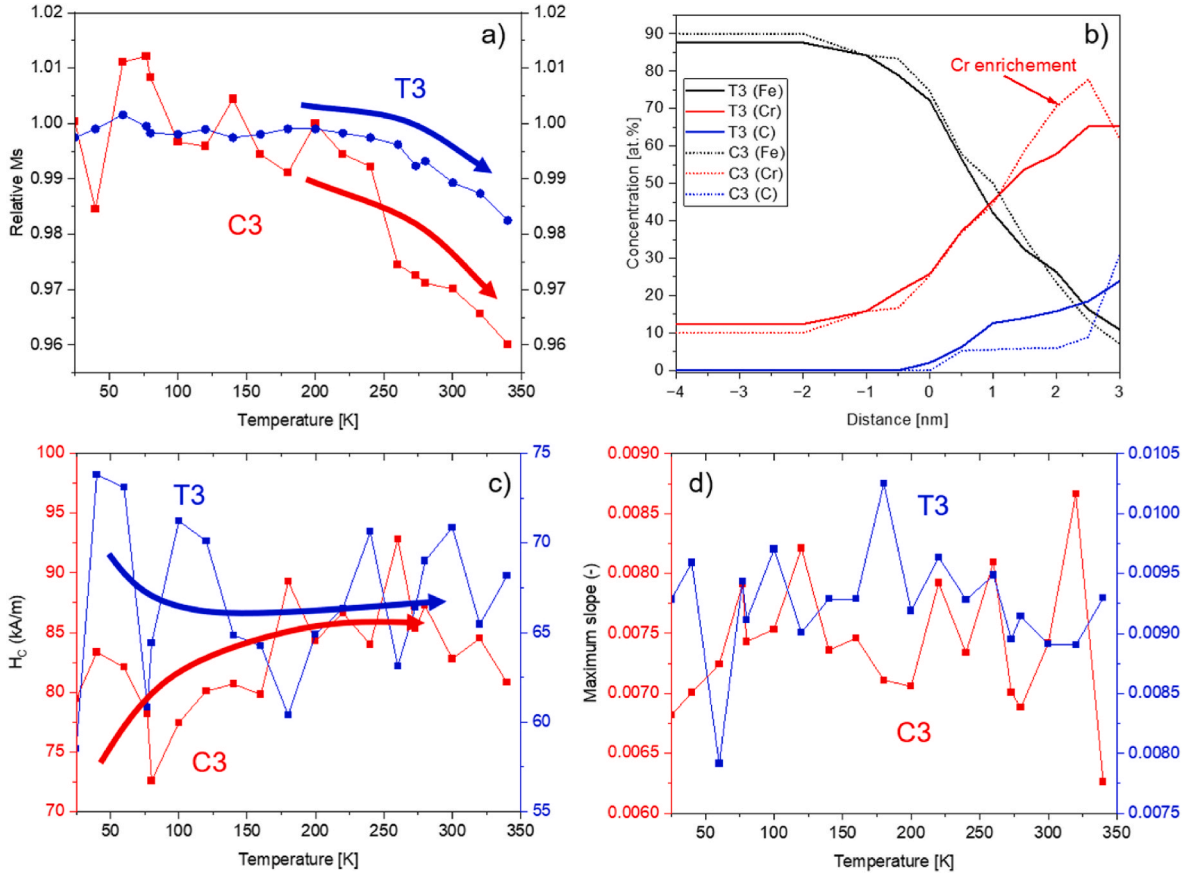

Fig. 6. Extracted information a) relative change of magnetic saturation (M_s), b) APT results of Fe, Cr and C concentrations based on study [17], c) coercive field (H_c), d) maximum slope in the hysteresis of the series of in-situ measured magnetic hysteresis of both C3 and T3 samples with temperature.

with the presence of non-equilibrium defects that in this study can be associated to the higher residual tensile stresses of C3 that with CP are removed in the case of T3. Furthermore, in the same study, APT analysis was also carried out and it was found that a discontinuity of C and N occurs in the Cr enrichments with respect to the Cr–Fe trend, corroborating with the observations of this study. Overall, the previous literature and our results strongly support the proposed theory of Cr-rich cluster suppression with CP via modification of Cr binding, defect reformation, carbide precipitation, chemical homogenization and structural relaxation of Eurofer97.

Another aspect in regards to M_s is also the scattering of the data that is considerably less prominent for T3 than for C3. The possible explanation is considered to be related to the homogeneity of the matrix phase that enables lower dispersion of the Kerr signal with encompassing varying grains that occurs due to the local drifting of the laser position on the sample. This in turn screens different sections of the sample with different domains and thus intermediate magnetic states that can influence the M_s in relation to local chemistry or structural parameters (i.e. Cr-enrichment). This goes hand in hand with the perspective of the higher homogeneity and reduced stress state of the material with CP as observed in this work and previous studies [17,31,39,51]. The variation due to the drifting position of the laser signal is visible from the H_c (see Fig. 6c) that shows for both samples similar scattering between different temperature points. Despite this, it is clear that T3 presents on average a lower H_c compared to C3 (83 mT against 105 mT) as seen already from the overall investigation of the hysteresis. Additionally, the H_c presents a differing trend in dependency of the temperature between C3 and T3 as indicated by the arrows in Fig. 6c. For T3, a slight decrease of H_c, which follows well the trend of thermally-induced agitation of the material. However, for C3 a slight increase of H_c is determined by about 10 mT with increasing temperature, which is speculated to originate from the aforementioned Cr clustering that inhibits antiferromagnetic coupling of them with the Fe matrix at temperatures below the Néel temperature that would explain the reduced H_c with lower temperature.

The temperature variation is also imprinted onto the slope of the hysteresis regime that occurs after the opening that can be seen from the maximum slope plotted in Fig. 6d. The maximum slope was obtained from the first derivative of the hysteresis, which is presented in Supplementary Material 8. Overall, no significant trend of the slope with temperature is found, indicating that both materials exhibit a similar maximum susceptibility in the measured temperature range. This is confirming that the relative M_s differences between C3 and T3 originate from changes in the local chemistry or presence of clusters and not from the in-situ effect of the cooling on the stress state of the material or other extrinsic effects. With the in-situ results it can be concluded that with CP Eurofer97 exhibits a generally more stable magnetic response with temperature variation and that the CP effectively modifies the local chemistry and phase formations that inadvertently influence the inherent magnetic properties in comparison when no CP is applied. With such relation to the microstructure, the magnetic properties can be used to predict the mechanical properties of Eurofer97 in a non-destructive manner and to predict the potential stability of Eurofer97 to high-energy radiation exposure.

4. Conclusions

This work investigates the effect of cryogenic processing (CP) on the selected properties of Eurofer97/2. The overall CP-induced changes of Eurofer97 indicate a more stable to changes and homogenized microstructure with a sufficiently equivalent ensemble of mechanical properties that indicate a potential to be used in current fission and future fusion reactor applications that require high material stability to microstructural changes induced by high-energy neutrons. The effect of CP is also studied in relation to different heat treatment parameters, such as tempering temperature (350 °C, 450 °C and 550 °C), which gives an insight to the influence of tempering on the CP performance and induced changes.

The study concludes the following effects of CP on Eurofer97.

1. The microstructural changes induced by CP confirm the successful transformation of FCC phase into BCC phase, transformation of Cr-rich intermetallic σ-phase into precipitates and Cr-rich BCC phase and consequently increased formation of refined carbides, such as $M_{23}C_6$. The analysis of micro-residual stresses shows the changes of tensile residual stresses to more compressive character for all investigated CP samples.
2. Observations of mechanical behaviour show a slight increase in microhardness after application of CP for all studied subgroups. The decrease of the impact toughness can be explained by a slight increase in the microhardness for all CP samples and an increase in BCC phase and a higher fraction of carbides.
3. CP modifies the magnetic properties by generally increasing the magnetic hardness and increase coercivity of Eurofer97 that is correlated to reduced tensile residual stresses and refined microstructure that results in finer magnetic domains and higher partitioning of magnetic regions with similar local magnetization change with the application of external magnetic field.
4. In-situ changes of magnetic hysteresis with cryogenic temperatures confirm the CP-induced chemical and microstructural changes that relate to a modified magnetic saturation and coercivity dependency with temperature. The changes are correlated to the higher homogeneity of the material and the suppression of formation of Cr-rich nanoclustering that is determined to be inherently present in Eurofer97 under conventional (without CP) processing conditions.
5. The mechanism for the stabilized microstructure is proposed to be related to the suppression of Cr-rich cluster formation with CP via modification of Cr binding, defect reformation, carbide precipitation, chemical homogenization and structural relaxation of Eurofer97.

CRediT authorship contribution statement

Matic Jovičević-Klug: Methodology, Validation, Formal analysis, Investigation, Writing – original draft, Writing – review & editing. **Carlo Alberto Brondin:** Methodology, Validation, Formal analysis, Investigation, Writing – original draft, Writing – review & editing, Resources. **Antonio Caretta:** Methodology, Investigation, Writing – original draft, Writing – review & editing, Resources. **Carsten Bonnekoh:** Methodology, Writing – original draft, Writing – review & editing, Resources. **Florian Gossing:** Methodology, Writing – original draft, Writing – review & editing. **Alexandra Vogel:** Methodology, Writing – original draft, Writing – review & editing. **Michael Rieth:** Writing – review & editing, Resources, Supervision. **Jeffrey McCord:** Writing – review & editing, Resources, Supervision. **Michael Rohwerder:** Writing – review & editing, Resources, Supervision. **Patricia Jovičević-Klug:** Conceptualization, Methodology, Validation, Formal analysis, Investigation, Writing – original draft, Writing – review & editing, Visualization, Resources.

Data availability

The raw and processed data required to reproduce these findings are available from the corresponding author upon request.

Funding

This study was mainly funded by Alexander von Humboldt Foundation Postdoc Fellowship (2023–2024), which recipient was Patricia Jovičević-Klug.

Declaration of competing interest

The authors declare that they have no known competing financial interests or personal relationships that could have appeared to influence the work reported in this paper.

Acknowledgement

We would like to thank Benjamin Breitbach for performing the XRD analysis and Heidi Bögershausen for measurements of microhardness. Carlo Alberto Brondin acknowledges CERIC–ERIC internal project MAG-ALCHEMI for the UHV MOKE.

Appendix A. Supplementary data

Supplementary data to this article can be found online at https://doi.org/10.1016/j.jmrt.2025.05.176.

References

[1] Möslang A, Diegele E, Klimiankou M, Lässer R, Lindau R, Lucon E, Materna-Morris E, Petersen C, Pippan R, Rensman JW, Rieth M, Van Der Schaaf B, Schneider HC, Tavassoli F. Towards reduced activation structural materials data for fusion DEMO reactors. Nucl Fusion 2005;45:649. https://doi.org/10.1088/0029-5515/45/7/013.

[2] Sandim MJR, Farrão FU, Oliveira VB, Bredda EH, Santos AD, Dos Santos CAM, Sandim HRZ. Effect of tempering on the microstructure, electrical, and magnetic properties of Eurofer-97 steel. J Nucl Mater 2015;461:265–70. https://doi.org/10.1016/J.JNUCMAT.2015.03.020.

[3] Genée J, Berbenni S, Gey N, Lebensohn RA, Bonnet F. Particle interspacing effects on the mechanical behavior of a Fe–TiB2 metal matrix composite using FFT-based mesoscopic field dislocation mechanics. Adv Model Simul Eng Sci 2020;7:1–23. https://doi.org/10.1186/S40323-020-0141-Z/FIGURES/11.

[4] Renzetti RA, Sandim HRZ, Sandim MJR, Santos AD, Möslang A, Raabe D. Annealing effects on microstructure and coercive field of ferritic–martensitic ODS Eurofer steel. Mater Sci Eng, A 2011;528:1442–7. https://doi.org/10.1016/J.MSEA.2010.10.051.

[5] Mergia K, Boukos N. Structural, thermal, electrical and magnetic properties of Eurofer 97 steel. J Nucl Mater 2008;373:1–8. https://doi.org/10.1016/J.JNUCMAT.2007.03.267.

[6] Lu Z, Faulkner RG, Riddle N, Martino FD, Yang K. Effect of heat treatment on microstructure and hardness of Eurofer 97, Eurofer ODS and T92 steels. J Nucl Mater 2009:445–8. https://doi.org/10.1016/J.JNUCMAT.2008.12.152. 386–388.

[7] Fu J, Brouwer JC, Hendrikx RWA, Richardson IM, Hermans MJM. Microstructure characterisation and mechanical properties of ODS Eurofer steel subject to designed heat treatments. Mater Sci Eng, A 2020;770:138568. https://doi.org/10.1016/J.MSEA.2019.138568.

[8] Lebarbé T, Pétesch C, Muñoz-Garcia J. Standardization of eurofer material, a first step toward industrialization. Fusion Eng Des 2020;159:111793. https://doi.org/10.1016/J.FUSENGDES.2020.111793.

[9] Park DG, Moon EJ, Kim DJ, Chi SH, Hong JH. The change of saturation magnetization in neutron-irradiated low-alloy steel. Phys B Condens Matter 2003;327:315–8. https://doi.org/10.1016/S0921-4526(02)01777-5.

[10] Klimenkov M, Jäntsch U, Rieth M, Dürrschnabel M, Möslang A, Schneider HC. Post-irradiation microstructural examination of EUROFER-ODS steel irradiated at 300°C and 400°C. J Nucl Mater 2021;557:153259. https://doi.org/10.1016/J.JNUCMAT.2021.153259.

[11] Williams CA, Hyde JM, Smith GDW, Marquis EA. Effects of heavy-ion irradiation on solute segregation to dislocations in oxide-dispersion-strengthened Eurofer 97 steel. J Nucl Mater 2011;412:100–5. https://doi.org/10.1016/J.JNUCMAT.2011.02.029.

[12] Reali L, Boleininger M, Gilbert MR, Dudarev SL. Macroscopic elastic stress and strain produced by irradiation. Nucl Fusion 2021;62:016002. https://doi.org/10.1088/1741-4326/AC35D4.

[13] Materna-Morris E, Adelhelm C, Baumgärtner S, Dafferner B, Graf P, Heger S, Jäntsch U, Lindau R, Petersen C, Rieth M, Ziegler R, Zimmermann H, Karlsruhe F. Final Report on the EFDA Task STRUCTURAL MATERIAL EUROFER97-2, Characterization of Rod and Plate Material: Structural, Tensile, Charpy, and Creep Properties 2007.

[14] Duerrschnabel M, Jäntsch U, Gaisin R, Rieth M. Microstructural insights into EUROFER97 batch 3 steels. Nuclear Materials and Energy 2023;35:101445. https://doi.org/10.1016/J.NME.2023.101445.

[15] Klimenkov M, Jäntsch U, Rieth M, Möslang A. Correlation of microstructural and mechanical properties of neutron irradiated EUROFER97 steel. J Nucl Mater 2020;538:152231. https://doi.org/10.1016/J.JNUCMAT.2020.152231.

[16] Jovičević-Klug P, Prabhakar JM, Giesbrecht CK, Schwarz TM, Bonnekoh C, Rieth M, Rohwerder M. Hydrogen diffusion and trapping in a cryogenic processed high-Cr ferrous alloy. npj Mater Degrad 2024;8(1 8):1–9. https://doi.org/10.1038/s41529-024-00522-1 (2024.

[17] Jovičević-Klug P, Bonnekoh C, Jovičević-Klug M, Ambrožič B, Dražić G, Miłosz Z, Ma Y, McCarroll I, Breitbach B, Amati M, Gregoratti L, Rieth M, Rohwerder M. Designing advanced high-Cr ferrous alloys for next-generation energy applications through cryogenic processing. Appl Surf Sci 2024;665:160290. https://doi.org/10.1016/j.apsusc.2024.160290.

[18] Jovičević-Klug P, Rohwerder M. Sustainable new Technology for the improvement of metallic materials for future energy applications. Coatings (Oakv) 2023;13:1822. https://doi.org/10.3390/COATINGS13111822. 1822 13 (2023.

[19] Jovičević-Klug P, Jovičević-Klug M, Rohwerder M, Godec M, Podgornik B. Complex interdependency of microstructure, mechanical properties, fatigue resistance and residual stress of austenitic stainless steels AISI 304L. Materials 2023;16:2638. https://doi.org/10.3390/ma16072638.

[20] Jovičević-Klug P, Lipovšek N, Jovičević-Klug M, Mrak M, Ekar J, Ambrožič B, Dražić G, Kovač J, Podgornik B. Assessment of deep cryogenic heat-treatment impact on the microstructure and surface chemistry of austenitic stainless steel. Surf Interfaces 2022:102456. https://doi.org/10.1016/J.SURFIN.2022.102456.

[21] Jovičević-Klug P, Jovičević-Klug M, Thormählen L, McCord J, Rohwerder M, Godec M, Podgornik B. Austenite reversion suppression with deep cryogenic treatment: a novel pathway towards 3rd generation advanced high-strength steels. Mater Sci Eng, A 2023;873:145033. https://doi.org/10.1016/J.MSEA.2023.145033.

[22] Senthilkumar D. Deep cryogenic treatment of En 31 and En 8 steel for the development of wear resistance 2021;8:1769–76. https://doi.org/10.1080/2374068X.2021.1878696.

[23] Senthilkumar D. Influence of deep cryogenic treatment on hardness and toughness of En31 steel. Advances in Materials and Processing Technologies 2019;5:114–22. https://doi.org/10.1080/2374068X.2018.1530426.

[24] Jurči P, Dománková M, Ptačinová J, Pašák M, Kusý M, Priknerová P. Investigation of the microstructural changes and hardness variations of sub-zero treated Cr-V Ledeburitic tool steel due to the tempering treatment. J Mater Eng Perform 2018;27:1514–29. https://doi.org/10.1007/s11665-018-3261-6.

[25] Yang Z, Liu Z, Liang J, Yang Z, Sheng G. Elucidating the role of secondary cryogenic treatment on mechanical properties of a martensitic ultra-high strength stainless steel. Mater Char 2021;178:111277. https://doi.org/10.1016/J.MATCHAR.2021.111277.

[26] hui Li D, chao He W, Zhang X, guo Xiao M, hong Li S, yu Zhao K, sheng Yang M. Effects of traditional heat treatment and a novel deep cryogenic treatment on microstructure and mechanical properties of low-carbon high-alloy martensitic bearing steel. J Iron Steel Res Int 2021;28:370–82. https://doi.org/10.1007/s42243-020-00527-5.

[27] Jovičević-Klug P, Kasdorf Giesbrecht C, Prabhakar JM, Schwarz TM, Bonnekoh C, Rieth M, Rohwerder M. Understanding nanoscale oxide build up on EUROFER97. Corros Sci 2025;245:112691. https://doi.org/10.1016/j.corsci.2025.11269.

[28] Oxley P, Goodell J, Molt R. Magnetic properties of stainless steels at room and cryogenic temperatures. J Magn Magn Mater 2009;321:2107–14. https://doi.org/10.1016/J.JMMM.2009.01.002.

[29] Gómez-Ferrer B, Vila R, Jiménez-Rey D, Ortiz CJ, Mota F, García JM, Rodríguez A. In situ resistivity measurements of RAFM base alloys at cryogenic temperatures: the effect of proton irradiation. J Nucl Mater 2014;447:225–32. https://doi.org/10.1016/J.JNUCMAT.2014.01.016.

[30] Cristalli C, Tassa O, Bozzetto L, Pilloni L. Achievement of Ultrafine Grain structure by means of recrystallization treatments. J Nucl Mater 2022;568:153852. https://doi.org/10.1016/J.JNUCMAT.2022.153852.

[31] Jovicevic-Klug M, Jovicevic-Klug P, McCord J, Podgornik B. Investigation of microstructural attributes of steel surfaces through magneto-optical Kerr effect. J Mater Res Technol 2021;11:1245–59. https://doi.org/10.1016/J.JMRT.2021.01.106.

[32] Akhbarizadeh A, Amini K, Javadpour S. Effects of applying an external magnetic field during the deep cryogenic heat treatment on the corrosion resistance and wear behavior of 1.2080 tool steel. Mater Des 2012;41:114–23. https://doi.org/10.1016/j.matdes.2012.03.045.

[33] Argüelles A, Barbés F, Espeso JI, Garcia-Mateo C. Cryogenic study of the magnetic and thermal stability of retained austenite in nanostructured bainite. Sci Technol Adv Mater 2019;20:673–87. https://doi.org/10.1080/14686996.2019.1625722.

[34] Jovičević-Klug P, Lipovšek N, Jovičević-Klug M, Podgornik B. Optimized preparation of deep cryogenic treated steel and Al-alloy samples for optimal microstructure imaging results. Mater Today Commun 2021;27:102211. https://doi.org/10.1016/j.mtcomm.2021.102211.

[35] Hauk S. Structural and residual stress analysis by nondestructive methods. Amsterdam, the Netherlands: Elsevier; 1997. https://doi.org/10.1016/B978-0-444-82476-9.X5000-2.

[36] Eaton P, West P. Chapter 3 AFM modes. Oxford University Press; 2010. https://doi.org/10.1093/ACPROF:OSO/9780199570454.003.0003.

[37] McCord J. Progress in magnetic domain observation by advanced magneto-optical microscopy. J Phys D Appl Phys 2015;48:333001. https://doi.org/10.1088/0022-3727/48/33/333001.

[38] Schmidt F, Rave W, Hubert A. Enhancement of magneto-optical domain observation by digital image processing. IEEE Trans Magn 1985;21:1596–8. https://doi.org/10.1109/TMAG.1985.1064048.

[39] Jovičević-Klug P, Jovičević-Klug M, Tegg L, Seidler D, Thormahlen L, Parmar R, Amati M, Gregoratti L, Cairney JM, McCord J, Rohwerder M, Podgornik B. Correlative surface and bulk analysis of deep cryogenic treatment influence on high-alloyed ferrous alloy. J Mater Res Technol 2022;11–12:4799–810. https://doi.org/10.1016/j.jmrt.2022.11.075.

[40] Malvestuto M, Caretta A, Bhardwaj R, Laterza S, Parmigiani F, Gessini A, Zamolo M, Galassi F, Sergo R, Cautero G, Danailov MB, Demidovic A, Sigalotti P,

Lonza M, Borghes R, Contillo A, Simoncig A, Manfredda M, Raimondi L, Zangrando M. The MagneDyn beamline at the FERMI free electron laser. Rev Sci Instrum 2022;93. https://doi.org/10.1063/5.0105261.
[41] Sato K. Measurement of magneto-optical kerr effect using piezo-birefringent modulator. Jpn J Appl Phys 1981;20:2403–9. https://doi.org/10.1143/JJAP.20.2403/XML.
[42] Genuzio F, Giela T, Lucian M, Mentes TO, Brondin CA, Cautero G, Mazalski P, Bonetti S, Korecki J, Locatelli A. A UHV MOKE magnetometer complementing XMCD-PEEM at the Elettra Synchrotron. J Synchrotron Radiat 2021;28:995. https://doi.org/10.1107/S1600577521002885.
[43] Soldatov IV, Schäfer R. Advanced MOKE magnetometry in wide-field Kerr-microscopy. J Appl Phys 2017;122. https://doi.org/10.1063/1.5003719/145126.
[44] Jovicevic-Klug P, Jovicevic-Klug M, Podgornik B. Effectiveness of deep cryogenic treatment on carbide precipitation. J Mater Res Technol 2020;9:13014–26. https://doi.org/10.1016/J.JMRT.2020.09.063.
[45] Jovičević-Klug P, Guštin AZ, Jovičević-Klug M, Šetina Batič B, Lebar A, Podgornik B. Coupled role of alloying and manufacturing on deep cryogenic treatment performance on high-alloyed ferrous alloys. J Mater Res Technol 2022;18:3184–97. https://doi.org/10.1016/J.JMRT.2022.04.025.
[46] Jacob A, Povoden-Karadeniz E, Kozeschnik E. Revised thermodynamic description of the Fe-Cr system based on an improved sublattice model of the σ phase. Calphad (N Y) 2018;60:16–28. https://doi.org/10.1016/J.CALPHAD.2017.10.002.
[47] Diegele E, Andreani R, Lässer R, Van Der Schaaf B. European fusion materials research program - recent results and future strategy. Fusion Sci Technol 2005;47:829–35. https://doi.org/10.13182/FST05-A789.
[48] Jo YH, Choi WM, Sohn SS, Kim HS, Lee BJ, Lee S. Role of brittle sigma phase in cryogenic-temperature-strength improvement of non-equi-atomic Fe-rich VCrMnFeCoNi high entropy alloys. Mater Sci Eng, A 2018;724:403–10. https://doi.org/10.1016/J.MSEA.2018.03.115.
[49] Stornelli G, Di Schino A, Mancini S, Montanari R, Testani C, Varone A. Grain refinement and improved mechanical properties of EUROFER97 by thermo-mechanical treatments. Appl Sci 2021;11:10598. https://doi.org/10.3390/APP112210598. 10598 11 (2021.
[50] Shen Y, Zhou X, Shi T, Huang X, Shang Z, Liu W, Ji B, Xu Z. Sigma phases in an 11% Cr ferritic/martensitic steel with the normalized and tempered condition. Mater Char 2016;122:113–23. https://doi.org/10.1016/J.MATCHAR.2016.10.031.
[51] Jovičević-Klug P, Tegg L, Jovičević-Klug M, Parmar R, Amati M, Gregoratti L, Almasy L, Cairney JM, Podgornik B. Understanding carbide evolution and surface chemistry during deep cryogenic treatment in high-alloyed ferrous alloy. Appl Surf Sci 2023;610:155497. https://doi.org/10.1016/j.apsusc.2022.155497.
[52] Jovičević-Klug M, Ma Y, Jovičević-Klug P, Prabhakar JM, Rohwerder M, Raabe D. Thermal kinetics and nitriding effect of ammonia-based direct reduction of iron oxides. ACS Sustainable Chem Eng 2024;12:9882–96. https://doi.org/10.1021/acssuschemeng.4c02363.
[53] Tolouei E, Hurel V, Loucif A, Morin JB, Jahazi M. Influence of the as quenched state and tempering temperature on the final microstructure and hardness of a high strength medium carbon steel. Mater Chem Phys 2024;325:129765. https://doi.org/10.1016/J.MATCHEMPHYS.2024.129765.
[54] Lu Z, Faulkner RG, Riddle N, Martino FD, Yang K. Effect of heat treatment on microstructure and hardness of Eurofer 97, Eurofer ODS and T92 steels. J Nucl Mater 2009;386–388:445–8. https://doi.org/10.1016/J.JNUCMAT.2008.12.152.
[55] Klimenkov M, Lindau R, Materna-Morris E, Möslang A. TEM characterization of precipitates in EUROFER 97. Prog Nucl Energy 2012;57:8–13. https://doi.org/10.1016/J.PNUCENE.2011.10.006.
[56] Jovičević-Klug P, Puš G, Jovičević-Klug M, Žužek B, Podgornik B. Influence of heat treatment parameters on effectiveness of deep cryogenic treatment on properties of high-speed steels. Mater Sci Eng, A 2022;829:142157. https://doi.org/10.1016/j.msea.2021.142157.
[57] Zhirafar S, Rezaeian A, Pugh M. Effect of cryogenic treatment on the mechanical properties of 4340 steel. J Mater Process Technol 2007;186:298–303. https://doi.org/10.1016/J.JMATPROTEC.2006.12.046.
[58] Hou TP, Wu KM, Liu WM, Peet MJ, Hulme-Smith CN, Guo L, Zhuang L. Magnetism and high magnetic-field-induced stability of alloy carbides in Fe-based materials. Sci Rep 2018;8(1 8):1–10. https://doi.org/10.1038/s41598-018-20910-3 (2018.
[59] Vourna P, Ktena A, Tsarabaris P, Hristoforou E. Magnetic residual stress monitoring technique for ferromagnetic steels. Metals 2018;8:592. https://doi.org/10.3390/MET8080592. Page 592 8 (2018.
[60] Chapman JBJ, Ma PW, Dudarev SL. Dynamics of magnetism in Fe-Cr alloys with Cr clustering. Phys Rev B 2019;99. https://doi.org/10.1103/PhysRevB.99.184413.
[61] Arajs S, Rao KV, Astrom HU, De Young TF. Determination of Néel temperatures of binary chromium alloys from electrical resistivity data. Phys Scri 1973;8:109. https://doi.org/10.1088/0031-8949/8/3/006.
[62] Ishikawa Y, Tournier R, Filippi J. Magnetic properties of Cr rich Fe-Cr alloys at low temperatures. J Phys Chem Solid 1965;26:1727–45. https://doi.org/10.1016/0022-3697(65)90204-0.
[63] Fu CC, Lavrentiev MY, Soulairol R, Dudarev SL, Nguyen-Manh D. Low- and high-temperature magnetism of Cr and Fe nanoclusters in iron-chromium alloys. Phys Rev B Condens Matter 2015;91. https://doi.org/10.1103/PhysRevB.91.094430.
[64] Fedorov M, Wróbel JS, London AJ, Kurzydłowski KJ, Fu CC, Tadić T, Dudarev SL, Nguyen-Manh D. Precipitation of Cr-rich clusters in Fe-Cr alloys: effects of irradiation from first principles modeling and experimental observations. J Nucl Mater 2023;587:154715. https://doi.org/10.1016/J.JNUCMAT.2023.154715.